Research Article | Vol. 29, No. 18 / 30 Aug 2021 / Optics Express 28680
Optics EXPRESS

Improvement in the signal amplitude and bandwidth of an optical atomic magnetometer via alignment-to-orientation conversion

MAOHUA ZHU,[1,2,4] LI WANG,[2,3,4] JUN GUO,[1,2] XIUCHAO ZHAO,[2,3] XIANPING SUN,[2,3] CHAOHUI YE,[1,2,3] AND XIN ZHOU[2,3,*]

[1] School of Physics, Huazhong University of Science and Technology, Wuhan 430074, China
[2] Key Laboratory of Magnetic Resonance in Biological Systems, State Key Laboratory of Magnetic Resonance and Atomic and Molecular Physics, National Center for Magnetic Resonance in Wuhan, Wuhan Institute of Physics and Mathematics, Innovation Academy for Precision Measurement Science and Technology, Chinese Academy of Sciences – Wuhan National Laboratory for Optoelectronics, Wuhan 430071, China
[3] University of Chinese Academy of Sciences, Beijing 100049, China
[4] These authors contributed equally to this work
[*] xinzhou@wipm.ac.cn

Abstract: We evaluated the alignment-to-orientation conversion (AOC) at the cesium D1 line to improve a nonlinear magneto–optical rotation (NMOR) optical atomic magnetometer's signal amplitude and bandwidth. For the $6\,^2S_{1/2}\,F=3 \rightarrow 6\,^2P_{1/2}\,F'=4$ transition, the AOC-related NMOR achieves a 1.7-fold enhancement in signal amplitude compared to the conventional NMOR, benefiting from narrow linewidth and ultraweak power broadening. Therefore, an effective amplitude-to-linewidth ratio is maintained in the high-laser-power region. This method is beneficial for detecting high-frequency magnetic signals in nuclear magnetic resonance and biomagnetism, as the NMOR magnetometer bandwidth increases with laser power.

1. Introduction

Optical atomic magnetometers are one of the most sensitive sensors for detecting ultraweak magnetic fields, which are used for biomagnetism [1–5], optically detected nuclear magnetic resonance (NMR) [6–9], and fundamental physics [10]. Spin-exchange relaxation-free (SERF) optical atomic magnetometers [11] have an outstanding magnetic sensitivity below $1\,\mathrm{fT_{rms}}/\sqrt{\mathrm{Hz}}$ [12], and are used for measuring weak magnetic signals such as magnetoencephalographic signals [1] and indirect nuclear spin–spin coupling spectra at zero magnetic field [6]. However, the thermal insulation of SERF magnetometers, being indispensable owing to their high operating temperature (typically above 100 °C) [11,12], increases the detection distance to biological or low-boiling samples and results in the attenuation of magnetic signals ($B \propto r^{-3}$). Therefore, an atomic magnetometer with moderate operating temperature and high sensitivity is required. Another type of optical atomic magnetometer is based on nonlinear magneto–optical rotation (NMOR) [13]. Such a magnetometer can operate at room temperature [14,15] and a finite magnetic field far away from zero [16,17] because there is no need for rapid collisions between alkalis atoms. However, the absolute sensitivity of NMOR magnetometers is generally one or two orders of magnitude lower than that of SERF counterparts [15]. Therefore, many technologies and mechanisms have been developed to improve the sensitivity of NMOR magnetometers, such as wave mixing [18] and squeezed light [19,20]. These methods introduce another laser beam inconducive to the integration of a magnetometer.

Various mechanisms cause NMOR with a typical curve and linewidth. The NMOR caused by Bennett-structure effect [21] is attributed to the variation of the ground state population during optical pumping. Its linewidth is related to the spontaneous emission rate Γ (tens of megahertz).

#435841 https://doi.org/10.1364/OE.435841
Journal © 2021 Received 6 Jul 2021; revised 13 Aug 2021; accepted 13 Aug 2021; published 20 Aug 2021

Optics EXPRESS

The coherence effect that involves the creation and evolution of atomic polarization has a linewidth that is characterized by the rate of atomic depolarization γ (tens to thousands of hertz). The slope of NMOR curve at zero field represents the coefficient of the magnetometer output versus the target magnetic field, and it is a vital parameter that affects the sensor's sensitivity. For a dispersion NMOR curve, the amplitude-to-linewidth ratio (ALR) is equal to half the value of the slope. Therefore, the coherence effect is the typical NMOR mechanism used in magnetic field detection.

The mechanism of coherence effect in the scheme with a single laser beam, which is used for pumping and probing simultaneously, can be described in three stages [22]. First, in the "pumping" stage, linearly polarized light optically pumps the atoms into a polarization of alignment with linear dichroism. Second, in the "evolving" stage, the atomic alignment undergoes Larmor precession in a magnetic field and rotates. Third, in the "probing" stage, the laser polarization is rotated via the interaction with the aligned polarized atoms. The coherence of the atomic ensemble increases with laser intensity. Moreover, another NMOR mechanism related to alignment-to-orientation conversion (AOC) [23] occurs at high laser intensity. Under the condition of AOC, intense linearly polarized light causes the aligned polarized atoms to generate an induced dipole moment when the atoms undergo Larmor precession. At that moment, the atomic polarization is no longer in the state of alignment (corresponding to the linear dichroism) but is converted to a state mixed with the orientation, causing the emergence of circular birefringence.

The AOC-related NMOR at the D2 lines of rubidium and cesium have been investigated previously [23–26]. The AOC caused the reversal of rotation for the $F \rightarrow F + 1$ transition at high intensity [23,24], This reversal indicated that the main contribution of rotation is from the alignment atomic medium with dichroism to the orientation atomic medium with birefringence [23]. Many NMOR magnetometers that optimized the sensitivity work at the region of AOC. The effects of elliptical polarization and transverse magnetic fields on the AOC-related NMOR have been discussed [25]. The transition between an aligned and an oriented atomic sample can be observed by monitoring atomic radio-frequency spectra [26]. However, the curve of AOC-related of NMOR is usually covered by the coherence NMOR and is not striking. Therefore, the response capacity of the AOC-related NMOR, especially the signal amplitude and bandwidth, is an important topic that requires further investigation.

Herein, we utilized the AOC mechanism in NMOR to enhance the signal detection of an optical atomic magnetometer. We evaluated the AOC-related NMOR in the D1 transition of cesium at a high laser power region. To optimize the AOC-related NMOR, the effects of laser power and detuning were investigated. With an increase in laser power, the AOC-related NMOR indicated an increased amplitude as well as a narrow linewidth, thereby resulting in a high ALR in the high-laser-power region. An exceptional reversal of rotation sign at $6\,^2S_{1/2}\,F = 4 \rightarrow 6\,^2P_{1/2}\,F' = 3$ transition. A theoretical evaluation based on nonperturbative density matrix calculations was performed to clarify the origin of the sign of laser polarization rotation in NMOR. Finally, owing to the improvement of the bandwidth at a high laser power, applications such as zero-field NMR and multinuclear NMR are discussed herein.

2. Principle

2.1. Experimental description

Figure 1 shows the diagram of the experimental apparatus. The cesium vapor cell (a cube with a side length of 10 mm) was paraffin coated to reduce the relaxation of the atom–wall collisions. The temperature of the cesium vapor cell was maintained at 37 °C with hot air and monitored using a PT100 thermometer. Five-layer magnetic shields (Mu metal, shielding factor of 10^5) were used to prevent the vapor cell from the disturbance of the geomagnetic field. A three-axis Helmholtz coils system was used to compensate for the residual magnetic field (nanotesla level).

Optics EXPRESS

In addition, this coils system could be used for the application of a scanning magnetic field to test the NMOR signal.

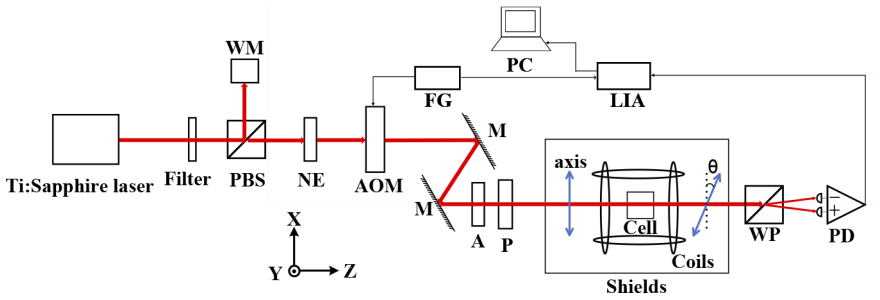

Fig. 1. Experimental setup. The diagram shows a single-beam scheme comprising a Ti:sapphire laser, an acousto–optic modulator (AOM), a lock-in amplifier (LIA), a mirror (M), a polarization beam splitter (PBS), a function generator (FG), an attenuator (A), a polarizer (P), Mu metal magnetic shielding layers (Shields), coils for shimming and pulsing (Coils), a ^{133}Cs vapor cell (Cell), a Wollaston prism (WP), a balanced photodetector (PD), and a computer system for programming control and data acquisition (PC), a wavelength meter (WM).

In this study, a Ti:sapphire laser system (Coherent, MR110) with characteristics of high power (2 W), wide-range continuous tunable wavelength (700 – 1030 nm), and narrow linewidth (<75 kHz) was applied. These characteristics are beneficial for evaluating the properties of the AOC-related NMOR. The laser frequency was locked through a Fabry–Pérot cavity and monitored using a wavemeter (Highfinesse, WS-6). The laser power was stabilized through a noise eater (Thorlabs, NEL03). An adjustable optical attenuator was used to control the power of the incident laser beam. The laser light propagating along the z-direction was linearly polarized along the x-direction via a polarizer before entering the vapor cell. The size of the laser beam is 0.46 mm^2. The rotation of the laser polarization was measured using a Wollaston prism and a balanced photodetector (New Focus 2307). To improve the SNR, the laser was amplitude modulated (Ω_m = 1800 Hz, 50% duty cycle and 100% modulated depth) by using an acousto–optic modulator and demodulated via a lock-in amplifier.

2.2. *Theory of light polarization rotation in AOC-related NMOR*

To describe the change in atomic polarization, the density matrix ρ is expanded with the polarization operators $\mathcal{T}^{\kappa q}$ as follows [27]:

$$\rho = \sum_{\kappa=0}^{2F} \sum_{q=-\kappa}^{\kappa} \rho_q^{\kappa} \mathcal{T}^{\kappa q}. \tag{1}$$

where κ is the rank of the polarization moments and ρ^0, ρ^1, and ρ^2 represent the monopole moment, dipole moment (orientation), and quadrupole moment (alignment), respectively. The polarization of atoms can be represented by the polarization moments.

Nonperturbative density matrix calculations [22] can be performed to evaluate the AOC-related NMOR. This theory was established by Budker and Rochester [27] and is suitable for both high and low laser powers. In this model, the rotation angle of the probe light is associated with the population of the ground-state atoms, which is related to the atomic density matrix ρ. The time-dependent evolution of the atomic density matrix ρ can be described via the Liouville

Optics EXPRESS

equation as follows [22]:

$$\dot{\rho} = -i\hbar^{-1}[H_0 + H_L + H_B, \rho] - \{\Gamma_R, \rho\}/2 + \Lambda. \tag{2}$$

where H_0 is the unperturbed Hamiltonian, H_L is the light–atom Hamiltonian, H_B is the magnetic-field–atom interaction Hamiltonian, Γ_R is the relaxation matrix, and Λ is the pumping matrix.

For the $F \rightarrow F \pm 1$ transitions, the rotation angle φ per unit distance for an optically thin medium can be written in the polarization tensor coordinator as follows:

$$\frac{d\varphi}{dz} = -\frac{2\pi\omega}{\varepsilon_0 c}\left(\left(\rho_{g,e}\right)_{q=+1}^{\kappa=1} + \left(\rho_{g,e}\right)_{q=-1}^{\kappa=1} + \left(\rho_{e,g}\right)_{q=+1}^{\kappa=1} + \left(\rho_{e,g}\right)_{q=-1}^{\kappa=1}\right). \tag{3}$$

where ω represents the laser frequency, ε_0 is the vacuum electric permittivity, c is the speed of light, g is the ground state, and e is the excited state. The ellipticity is neglected owing to the linearly polarized light. Equation (3) shows the contribution of the atomic polarization tensor of rank 1 between the ground and excited states to the rotation of the light polarization; additionally, it reflects the alignment and orientation of the atomic polarization.

3. Results and discussions

3.1. AOC at Cs D1 line

To interpret the AOC-related NMOR at high intensity, numerical simulations at the $6\,^2S_{1/2}\,F = 3 \rightarrow 6\,^2P_{1/2}\,F' = 4$ transition of the cesium D1 line were performed using the AtomicDensityMatrix package developed by Rochester and Budker [28]. The rotation of laser polarization with the magnetic field is shown in Fig. 2(a). The Doppler broadening effect was considered in the simulations by convolving the Doppler-free calculated results of different detuning with the Doppler distribution. Such treatment is reasonable as the atoms are pumping and probing simultaneously. The relaxation of the ground state is chosen at the level of tens of Hz to fit a cell system with paraffin coated. It should be noted that a "twist" structure [13,25] was clearly visible, as shown as the central red curve in Fig. 2(a). The insets in Fig. 2(a) show the probability surfaces [27] of the atomic polarization of the ground state at magnetic fields of −0.2 and 20 nT. The atomic polarization shows a superposition of the alignment and orientation in the "twist" structure at −0.2 nT. Further, we calculated the components of the emergent orientation and alignment, as shown in Fig. 2(b-d). The horizontal scales in Fig. 2(b-d) are from −5 nT to 5 nT for the clear show of the polarization components around the "twist" structure. When the magnetic field is outside the "twist" structure, the orientation component ρ_0^1 are almost zero, and the alignment component ρ_0^2 is on the level of 0.04, indicating the alignment domain region. For a better comparison, the "twist" structure is for the AOC-related NMOR, whereas the wider curve is for the conventional NMOR. Evidently, the AOC-related NMOR achieves a higher ALR.

Subsequently, we measured the magnetometer response to a series of magnetic fields along the z-axis (B_z-fields) for the two proposed types of NMOR signals. The laser power was 0.5 mW, and the frequency was selected at the center of the $6\,^2S_{1/2}\,F = 3 \rightarrow 6\,^2P_{1/2}\,F' = 4$ transition. Two types of NMOR appeared corresponding to the different mechanisms, as shown in Fig. 3(a). The ALRs for the AOC-related and conventional NMOR were 0.60 mrad/nT and 0.04 mrad/nT, respectively. They can be used to characterize the magnetometer response. Furthermore, the responses to alternating current (AC) magnetic signals were measured and compared. An additional sinusoidal magnetic field with an amplitude of 38 pT (rms value) and a frequency of 80 Hz was applied in the z-direction to quantify the response of the magnetometer. The response amplitude of the magnetometer to this AC magnetic field was obtained through a discrete Fourier transformation. As shown in Fig. 3(b), the AC response varied with the different static B_z offset. The central peak corresponded to the AOC-related NMOR, and the two side peaks corresponded to the conventional NMOR. The asymmetry of the two side peaks could

Optics EXPRESS

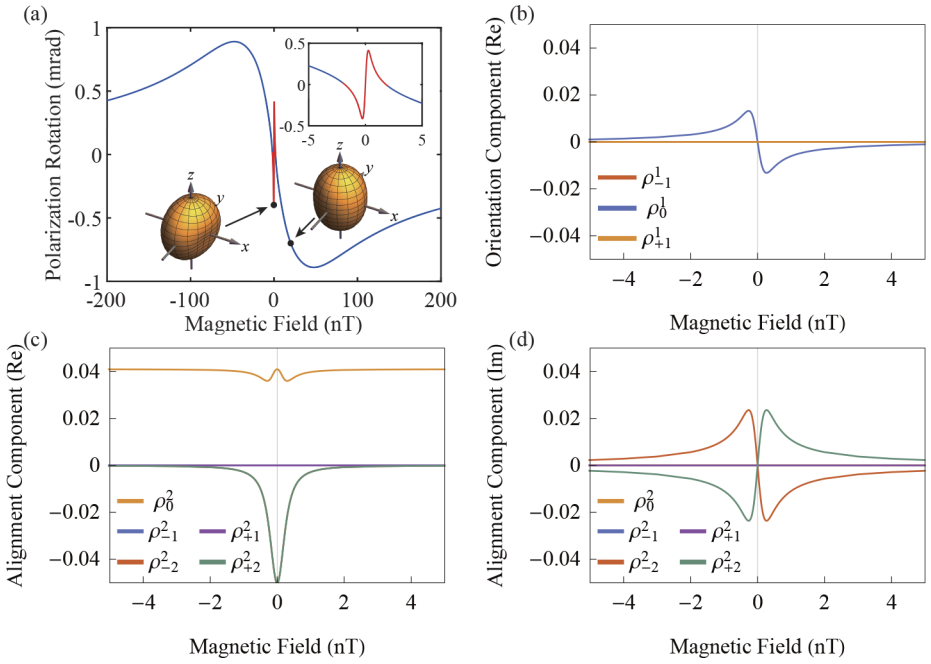

Fig. 2. Numerical calculations for the $6\,^2S_{1/2}\,F = 3 \rightarrow 6\,^2P_{1/2}\,F' = 4$ transition of the cesium D1 line. (a) Polarization rotation varies as a function of the magnetic field. The light propagation direction was chosen as the quantization axis. The direction of magnetic field and light propagation is parallel. The insets show the probability surfaces of the atomic polarization at different magnetic fields and the polarization rotation around 0 nT. (b) Atomic orientation polarization components. The imaginary part is zero. (c-d) Real and imaginary parts of the atomic alignment polarization components, respectively. The curves of $\rho^2_{\pm1}$ in (b), $\rho^2_{\pm1}$ and $\rho^2_{\pm2}$ in (c), and $\rho^2_{\pm1,0}$ in (d) overlap. Atomic polarization components vary as a function of the magnetic field. The calculations show the change of the atomic polarization domain region from the aligned to the oriented state in the low-magnetic-field range, thus resulting in a narrow AOC-related NMOR signal. The calculated parameters are laser intensity: 0.2 mW/cm^2, and rate of atomic depolarization: $\gamma = 2\pi \times 1.59\,s^{-1}$.

be caused by the transverse magnetic field [13,25]. The maximum AC signal response in the AOC region was 0.428 mrad/nT, which was a 1.7 fold enhancement of the value (0.159 mrad/nT) in the coherence region (B_z = 11 nT). We also measured the noise of the magnetometer in the absence of AC magnetic field. The noise was almost constant as a function of the offset magnetic field with slightly higher intensities in the AOC region.

To evaluate the effect of laser detuning, the NMOR signals with a laser frequency from 335.1103 to 335.1223 THz were measured at an incident laser power of 0.5 mW. The analyzed results are shown in Fig. 4(a-c). At this laser power, the AOC effect only occurred around the $6\,^2S_{1/2}\,F = 3 \rightarrow 6\,^2P_{1/2}\,F' = 4$ transition. As shown in Fig. 4(a), the amplitudes of the AOC- and conventional NMOR curve are at the same level. However, the linewidths of the AOC-related NMOR are almost one order narrower than those of the conventional NMOR, as shown in Fig. 4(b). The significant reduction in the linewidth resulted in a higher ALR, as shown in Fig. 4(c). The ALR of the AOC-related NMOR at the $6\,^2S_{1/2}\,F = 3 \rightarrow 6\,^2P_{1/2}\,F' = 4$ transition is lower than the ALR around the $6\,^2S_{1/2}\,F = 4 \rightarrow 6\,^2P_{1/2}\,F' = 3$ transition at 0.5 mW. However, the AOC-related NMOR has an ALR advantage at higher laser power region, as shown in Fig. 4(d).

Optics EXPRESS

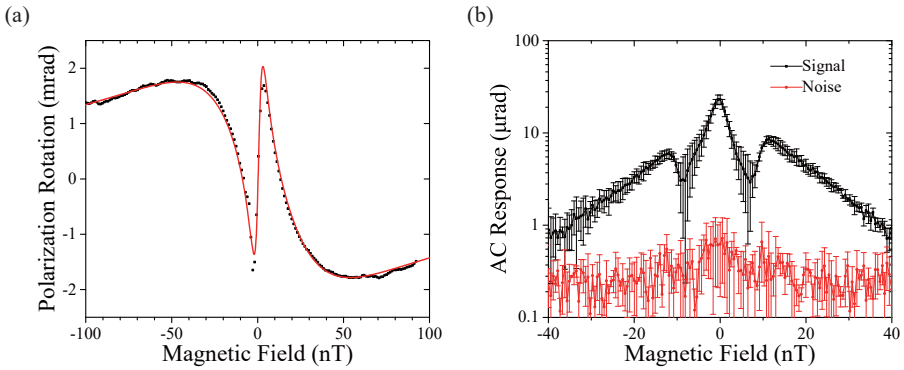

Fig. 3. Response of the optical atomic magnetometer. The incident laser power was 0.5 mW before entering the magnetic shields. The laser frequency was set at the center of the $6\,^2S_{1/2}\,F = 3 \rightarrow 6\,^2P_{1/2}\,F' = 4$ transition. (a) The optical rotation angle of the laser polarization to a series of longitudinal B_z magnetic fields, depicting the NMOR signal with a "twist" structure. The dots represent experimental data, and the line represents the fitting curve. (b) Response of the magnetometer to a sinusoidal magnetic field at different B_z offsets. The noise is one order lower than the response amplitude. The response amplitude in the AOC region was higher than that in the coherence region.

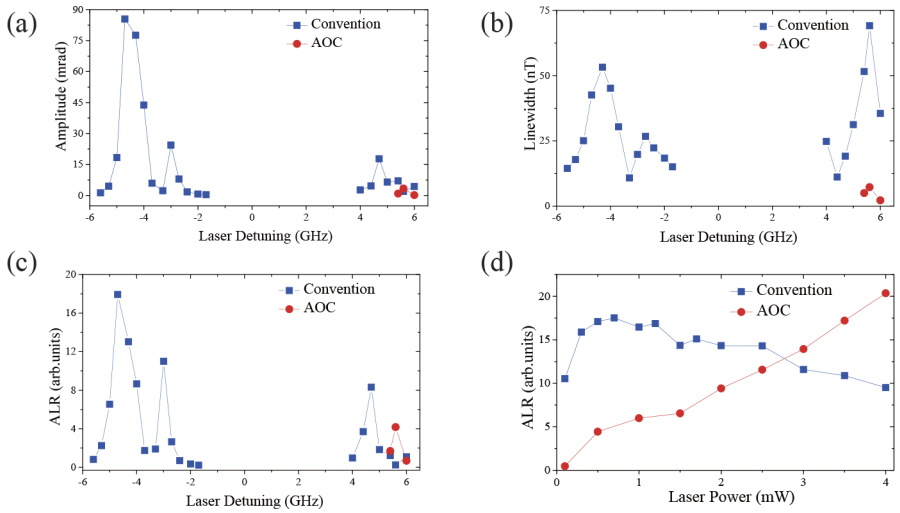

Fig. 4. Results obtained from the measurements of NMOR curves under different laser detuning. (a) Amplitude; (b) linewidth; and (c) ALR. The laser detuning $\Delta = 0$ GHz corresponds to the center of the cesium D1 transition. For a laser power of 0.5 mW, the AOC-related NMOR appeared near the $6\,^2S_{1/2}\,F = 3 \rightarrow 6\,^2P_{1/2}\,F' = 4$ transition. (d) The results of the ALR vary as a function of laser power. The convention NMOR is the results of the $6\,^2S_{1/2}\,F = 4 \rightarrow 6\,^2P_{1/2}\,F' = 3$ transition. The AOC NMOR is the results of the $6\,^2S_{1/2}\,F = 3 \rightarrow 6\,^2P_{1/2}\,F' = 4$ transition. The results of higher laser power show that the ALR of AOC-related NMOR is higher than the ALR of conventional NMOR at the $4 \rightarrow 3$ transition.

Detailed results about the effect of laser power on the NMOR signals are summarized in Fig. 5. The first experiment was performed at the transition of $6\,^2S_{1/2}\,F = 3 \rightarrow 6\,^2P_{1/2}\,F' = 4$ (Figs. 5(a,c,d)), corresponding to $F \rightarrow F + 1$. Figure 5(a) shows the polarization rotation of

Optics EXPRESS

the laser dependence on the B_z magnetic field at different laser powers. As the laser power was increased, the amplitude of the AOC-related NMOR increased owing to the growth of the induced dipole. Meanwhile, the conventional NMOR showed decreasing and broadening trends, and vanished at laser powers above 5 mW. One feature of the AOC in NMOR is that the sign of rotation of $F \rightarrow F + 1$ is opposite at low and high laser intensity. The experimental results of laser power in Fig. 5(a) show the change of the rotation sign owning to the growing AOC-related NMOR signals with laser power. These experimental results are consistent with the feature of AOC in NMOR.

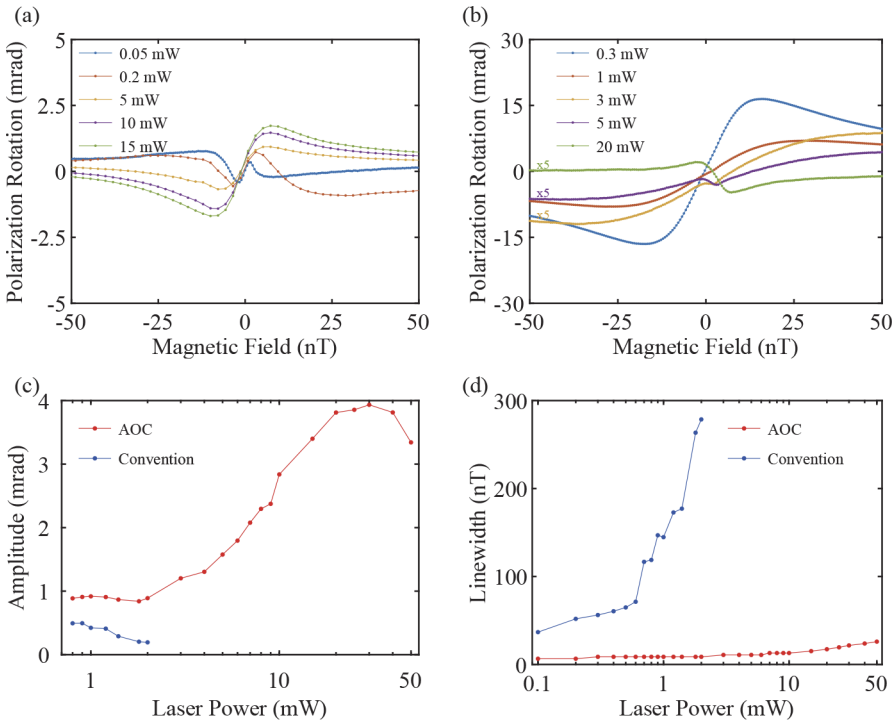

Fig. 5. Experimental results of the NMOR signal at different laser powers. (a) Polarization rotation of the laser dependence on the longitudinal B_z magnetic field at the transition of $6\,^2S_{1/2}\,F = 3 \rightarrow 6\,^2P_{1/2}\,F' = 4$. The sign reversal occurs at low laser power (below 0.05 mW). (b) Polarization rotation of the laser dependence on the longitudinal B_z magnetic field at the transition of $6\,^2S_{1/2}\,F = 4 \rightarrow 6\,^2P_{1/2}\,F' = 3$. The rotation reversal occurred at high laser powers (above 3 mW). The lines were scaled for better visibility. (c) Amplitude and (d) linewidth of NMOR versus laser power at the transition of $6\,^2S_{1/2}\,F = 3 \rightarrow 6\,^2P_{1/2}\,F' = 4$.

Further analysis of NMOR curves in Fig. 5(c) shows that the amplitude of the conventional NMOR signal decreased as the laser power was increased from 0.8 to 2 mW. In contrast, the amplitude of the AOC-related NMOR increased monotonically as the laser power was increased from 0.8 to 30 mW; subsequently, it decreased at higher powers. Figure 5(d) shows the results of NMOR linewidth versus laser power. The linewidth of the AOC-related NMOR was on the level of 9 nT (equivalent to 31.5 Hz for cesium atoms, $\Delta\nu = \Delta B \cdot \gamma_{Cs}$, $\gamma_{Cs} = 3.5$ Hz/nT) in the power range from 0.1 to 2 mW, which was significantly narrower than that of the conventional NMOR. Additionally, with an increase in the laser power, the linewidth of the AOC-related NMOR broadened more slowly than that of the conventional NMOR. The laser broadening

Optics EXPRESS

coefficients of the two types of NMOR signals obtained via linear fitting with the laser power were 1.37 Hz/mW and 459.56 Hz/mW for the AOC- and conventional NMORs, respectively.

The second experiment was performed at the transition of $6\,^2S_{1/2}\,F = 4 \rightarrow 6\,^2P_{1/2}\,F' = 3$ (corresponding to the $F \rightarrow F - 1$ transition). Figure 5(b) shows the results of NMOR signals at different laser powers. In addition, a reversal of the NMOR signal at a high laser power was observed. Such reversal at high laser power differs from the result of the rubidium D2 line [23,24], where the flip of the rotation sign causing by AOC only occurred at the $F \rightarrow F + 1$ transition. More calculations have been done to explain the reversal of rotation sign with laser power in the next subsection.

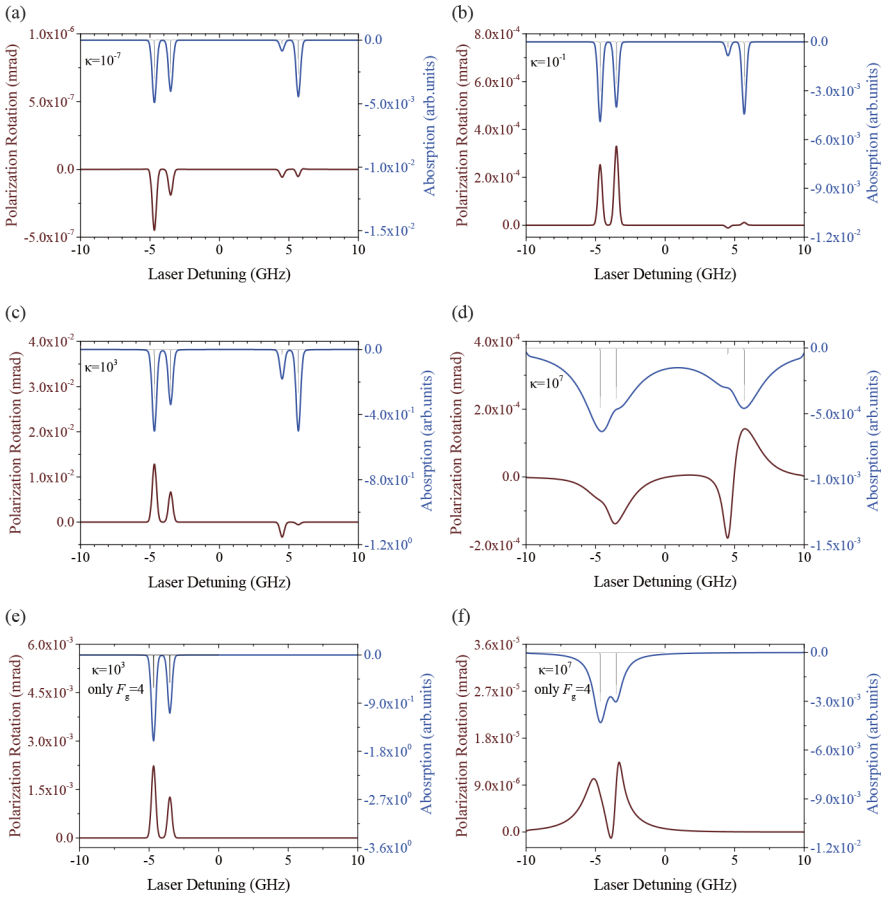

Fig. 6. Numerical calculations of the laser polarization rotation and absorption as a function of the laser frequency detuning with the Doppler effect. (a) $\kappa = 10^{-7}$, linear Faraday effect domain region; (b) $\kappa = 10^{-1}$, coherence effect domain region; (c) $\kappa = 10^3$ and (d) $\kappa = 10^7$, AOC effect domain region; (e) $\kappa = 10^3$ and (f) $\kappa = 10^7$, with single ground state $F_g = 4$. The black lines inside the absorption curves indicate the frequency of D1 transitions. The detuning $\Delta = 0$ GHz corresponds to the center of the cesium D1 line. The rotation sign is determined by various magneto-optical effects with different κ value. The calculated parameters are: $\gamma = 2\pi \times 15.9\,s^{-1}$, $B_z = 0.1$ nT, and $T = 25\,^\circ$C.

Optics EXPRESS

3.2. Calculation for the relation between the rotation sign and laser power

Consider the case of the cesium D1 line, a system with four ground and excited states hyperfine sublevels. The calculated results of the polarization rotations as a function of the laser frequency detuning are shown in Fig. 6. The Doppler effect was also considered in the calculation. The saturation parameter $\kappa = \Omega_R^2/(\Gamma\gamma)$ was introduced to characterize the laser power effects. The parameter Ω_R is the Rabi frequency and the Γ is the relaxation rate of the transition. The comparison of polarization rotation in Figs. 6(a) and 6(b) reveal the change of rotation sign at the low κ range from 10^{-7} to 10^{-1}. This reversal can be illustrated via a closed transition $F = 1 \rightarrow F' = 0$, because the domain effect changes from a linear Faraday to a coherence effect, as shown in Supplement 1, Fig. S1. Figure 6(b) also shows a typical feature of the coherence effect domain region that the signs of laser polarization rotation at the $F \rightarrow F$ and $F \rightarrow F1$ transitions are the same, and are opposite to the sign at the $F \rightarrow F + 1$ transition [23]. Another reversal of the rotation sign at $6\,^2S_{1/2}\,F = 3 \rightarrow 6\,^2P_{1/2}\,F' = 4$ transition emerges with the increase in κ, as shown in Figs. 6(b) and 6(c). This phenomenon is caused by the AOC effect and is consistent with the previous results [23]. Figure 6(d) shows the results of $\kappa = 10^7$, where the hyperfine transitions become partially resolved [29], subject to the combinational effect of the AC Stark shift and Doppler effects. An interesting reversal of the rotation sign for the $6\,^2S_{1/2}\,F = 4 \rightarrow 6\,^2P_{1/2}\,F' = 3$ transition occurs. This reversal contradicts the results that the contributions of laser polarization rotation from the linear dichroism and the circular birefringence at $F \rightarrow F - 1$ transition have the same sign [23], signifying the existence of other mechanisms. Results in Figs. 6(e) and 6(f) indicate that such a reversal does not occur in the case of a single ground state.

To address the effect of hyperfine sublevels at relatively high κ, the rotation of laser polarization was decomposed to the components from the ground- and excited-states hyperfine sublevels, $\varphi_{\text{total}} = \varphi_{F_g=3,F_e=3} + \varphi_{F_g=3,F_e=4} + \varphi_{F_g=4,F_e=3} + \varphi_{F_g=4,F_e=4}$, as shown in Fig. 7. Herein, the term φ_{F_g,F_e} is contributed from the phase shift of σ_+ and σ_- between F_g and F_e. The Doppler-free case was used to show the details. The $6\,^2S_{1/2}\,F = 4 \rightarrow 6\,^2P_{1/2}\,F' = 3$ transition was chosen specially to study. In the case of the relatively high κ ($= 10^7$), the calculated rotation of laser polarization with the magnetic field is shown in Fig. 7(a). A "twist" structure similar to the experimental results shown in Fig. 4(b) appears. The wide structure was broadened by the laser intensity. At such high κ, the majority of atoms were pumped out from the initial hyperfine sublevel and repopulated to another hyperfine sublevel under the spontaneous emission, thus making the transition no longer closed. Therefore, the contributions attributed to other hyperfine sublevels emerge as shown in Fig. 7(c). The main contribution at 0.1 nT is $\varphi_{F_g=3,F_e=4}$ that leads to a negative rotation. This phenomenon depends on the magnetic field strength. Thus, when the magnetic field increases to 200 nT, the main contribution comes from the $F_g = 4$ hyperfine sublevel, and the sign of the rotation becomes positive, as shown in Fig. 7(d). In comparison, in the case of the lower κ ($= 10^3$), the contribution owing to other hyperfine sublevels can be neglected. Therefore, the rotation sign is positive, as shown in Fig. 7(b). Accordingly, the rotation reversal for $6\,^2S_{1/2}\,F = 4 \rightarrow 6\,^2P_{1/2}\,F' = 3$ transition at relatively high κ is attributed to the combinational effect of AOC and hyperfine sublevels. Such a phenomenon can occur at laser power level of milliwatts in a low γ system. For example, to realize the $\kappa = 10^3$ and $\kappa = 10^7$ in this calculation, the laser intensities were approximately 2.9 μW/cm^2 and 29 mW/cm^2, respectively.

3.3. Discussion

Next, we discuss the applications of AOC-related NMOR. Our experimental results show that the AOC effect results in a higher ALR than the coherence owing to the narrower linewidth, thereby improving the sensitivity of the optical atomic magnetometer. Moreover, the AOC-related NMOR can be used for the detection of high-frequency magnetic fields (e.g., hundreds of hertz).

Optics EXPRESS

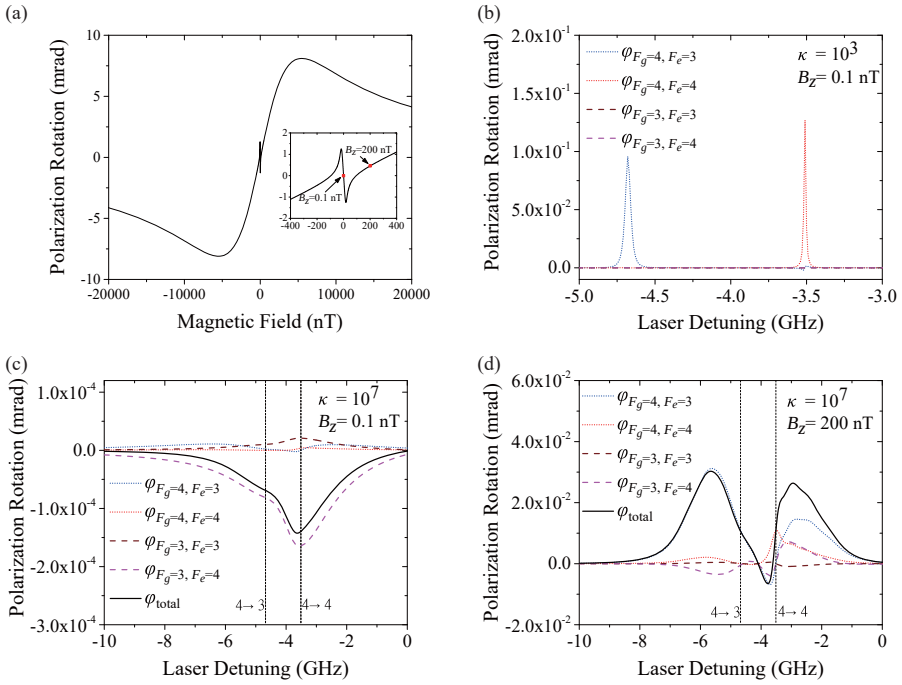

Fig. 7. Numerical calculations for the effect of hyperfine ground state in the absence of the Doppler effect. (a) Polarization rotation variation as a function of the magnetic field of the $6\,^2S_{1/2}\,F = 4 \rightarrow 6\,^2P_{1/2}\,F' = 3$ transition at $\kappa = 10^7$. The inset shows the polarization rotation around the zero magnetic field. (b-d) Laser polarization rotation variation as a function of laser detuning at (b) $\kappa = 10^3$, $B_z = 0.1\,\text{nT}$, (c) $\kappa = 10^7$, $B_z = 0.1\,\text{nT}$, and (d) $\kappa = 10^7$, $B_z = 200\,\text{nT}$, respectively. In the relatively low κ range ($<10^3$), the main contributions to the rotation of laser polarization are attributed to the corresponding transition line. The transition can be assumed to be a closed transition. Meanwhile, the effect of hyperfine ground state emerges in the relatively high κ ($\sim 10^7$) region. The γ value in the calculations is $2\pi \times 15.9\,\text{s}^{-1}$.

Importantly, the response bandwidth of the NMOR magnetometer can be improved by almost one order of magnitude by increasing the laser power to 20 mW, as shown in Fig. 8. However, increasing the laser power broadened the signal linewidth of the conventional NMOR and then decreased the sensitivity, as shown in Fig. 5. In contrast, the NMOR signal related to the AOC effect could maintain an effective response to the magnetic signal in the high-laser-power region. Hence, the evaluations of AOC-related NMOR are significant to the measurement of zero-field NMR, where the J-coupling (~ hundreds of hertz [6]) effect dominates. A higher field (approximately tens of microtesla) for multinuclear NMR necessitates a larger magnetometer bandwidth. Furthermore, magnetometers with extended bandwidth (temporal resolution) can also find useful applications in the detection of fast-varying biomagnetic signals, such as P-waves, QRS-complexes, and T-waves (up to 200 Hz [2]) in magnetocardiograms.

A major limitation of AOC-related NMOR is that it is highly sensitive to the transverse magnetic field. On one hand, the transverse magnetic field will cause the dampening, broadening, and asymmetry of the AOC-related NMOR curve, leading to a significant decrease in the response amplitude of signals. Thus, magnetic shielding and compensation of the residual magnetic field should be carefully considered. On the other hand, it can be used to shim the residual magnetic field. The atomic velocities were assumed to be invariant with Maxwell distribution

Optics EXPRESS

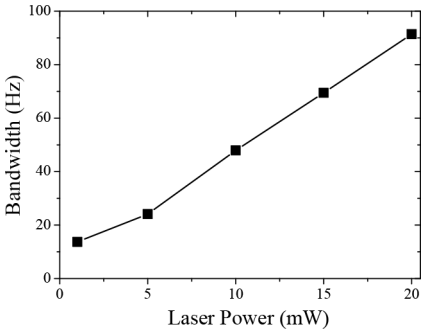

Fig. 8. Experiment results of −3 dB bandwidth versus laser power. The laser frequency is set to the center of the $6\,^2S_{1/2}\,F = 3 \rightarrow 6\,^2P_{1/2}\,F' = 4$ transition.

in our nonperturbative density matrix calculation. This theoretical treatment is succeeded in clarifying the relationship between the sign of laser polarization rotation and laser intensity, as demonstrated in the case described in Figs. 6 and 7. Further, some factors are neglected in our calculations, such as wall effect, spin-exchange and spin-destruction due to collisions. These factors should be considered for precisely evaluation in future.

4. Conclusion

We have proposed an optical atomic magnetometer based on the AOC mechanism working at the cesium D1 transition. The effects of laser power and frequency on the response amplitude and bandwidth of the magnetometer were evaluated. The response amplitude of the AOC-related NMOR was 170% higher than that of the conventional NMOR at the $6\,^2S_{1/2}\,F = 3 \rightarrow 6\,^2P_{1/2}\,F' = 4$ transition. This was due to the narrow linewidth and ultraweak power broadening. The bandwidth of the magnetometer can be improved by almost one order of magnitude by increasing the laser power. Furthermore, the abnormal phenomenon of rotation reversal at the $6\,^2S_{1/2}\,F = 4 \rightarrow 6\,^2P_{1/2}\,F' = 3$ transition was observed owing to the AOC and hyperfine effect at high κ region. These variations were effectively explained by a theoretical model based on nonperturbative density matrix calculations. Overall, we conclude that the AOC-related NMOR at the cesium D1 line can be used to improve the sensitivity and bandwidth of NMOR atomic magnetometers. Moreover, it benefits practical applications such as NMR optical detection and biomagnetism, where measurements require high bandwidths and the ability to be performed at room temperature.

Funding. National Natural Science Foundation of China (91859206, 81625011, 21921004, 11905288); National Key Research and Development Program of China (2018YFA0704000); Key Research Program of Frontier Sciences, Chinese Academy of Sciences (ZDBS-LY-JSC004); Strategic Priority Research Program of Chinese Academy of Sciences (XDB21010200); Science and Technology Innovation Special Funding for East Lake National Laboratory.

Acknowledgments. X. Zhou acknowledges the support from the Tencent Foundation through the XPLORER PRIZE for this study.

Disclosures. The authors declare no conflicts of interest.

Data availability. The data underlying the results presented herein are not publicly available currently but can be obtained from the authors upon reasonable request.

Supplemental document. See Supplement 1 for supporting content.

References

1. E. Boto, N. Holmes, J. Leggett, G. Roberts, V. Shah, S. S. Meyer, L. D. Muñoz, K. J. Mullinger, T. M. Tierney, S. Bestmann, G. R. Barnes, R. Bowtell, and M. J. Brookes, "Moving magnetoencephalography towards real-world applications with a wearable system," Nature **555**(7698), 657–661 (2018).

Optics EXPRESS

2. K. Jensen, M. A. Skarsfeldt, H. Stærkind, J. Arnbak, M. V. Balabas, S.-P. Olesen, B. H. Bentzen, and E. S. Polzik, "Magnetocardiography on an isolated animal heart with a room-temperature optically pumped magnetometer," Sci. Rep. **8**(1), 16218 (2018).
3. E. Corsini, V. Acosta, N. Baddour, J. Higbie, B. Lester, P. Licht, B. Patton, M. Prouty, and D. Budker, "Search for plant biomagnetism with a sensitive atomic magnetometer," J. Appl. Phys. **109**(7), 074701 (2011).
4. G. Bison, R. Wynands, and A. Weis, "Dynamical mapping of the human cardiomagnetic field with a room-temperature, laser-optical sensor," Opt. Express **11**(8), 904 (2003).
5. R. Wyllie, M. Kauer, R. T. Wakai, and T. G. Walker, "Optical magnetometer array for fetal magnetocardiography," Opt. Lett. **37**(12), 2247–2249 (2012).
6. J. W. Blanchard, M. P. Ledbetter, T. Theis, M. C. Butler, D. Budker, and A. Pines, "High-resolution zero-field NMR J-spectroscopy of aromatic compounds," J. Am. Chem. Soc. **135**(9), 3607–3612 (2013).
7. D. A. Barskiy, M. C. D. Tayler, I. Marco-Rius, J. Kurhanewicz, D. B. Vigneron, S. Cikrikci, A. Aydogdu, M. Reh, A. N. Pravdivtsev, J.-B. Hövener, J. W. Blanchard, T. Wu, D. Budker, and A. Pines, "Zero-field nuclear magnetic resonance of chemically exchanging systems," Nat. Commun. **10**(1), 3002 (2019).
8. G. Liu, X. Li, X. Sun, J. Feng, C. Ye, and X. Zhou, "Ultralow field NMR spectrometer with an atomic magnetometer near room temperature," J. Magn. Reson. **237**, 158–163 (2013).
9. N. C. Garcia, D. Yu, L. Yao, and S. Xu, "Optical atomic magnetometer at body temperature for magnetic particle imaging and nuclear magnetic resonance," Opt. Lett. **35**(5), 661–663 (2010).
10. S. Pustelny, D. F. Kimball, C. Pankow, M. P. Ledbetter, P. Wlodarczyk, P. Wcislo, M. Pospelov, J. R. Smith, J. Read, W. Gawlik, and D. Budker, "The global network of optical magnetometers for exotic physics (GNOME): a novel scheme to search for physics beyond the standard model," Ann. Phys. **525**(8-9), 659–670 (2013).
11. J. C. Allred, R. N. Lyman, T. W. Kornack, and M. V. Romalis, "High-sensitivity atomic magnetometer unaffected by spin-exchange relaxation," Phys. Rev. Lett. **89**(13), 130801 (2002).
12. I. K. Kominis, T. W. Kornack, J. C. Allred, and M. V. Romalis, "A subfemtotesla multichannel atomic magnetometer," Nature **422**(6932), 596–599 (2003).
13. D. Budker, V. Yashchuk, and M. Zolotorev, "Nonlinear magneto-optic effects with ultranarrow widths," Phys. Rev. Lett. **81**(26), 5788–5791 (1998).
14. V. G. Lucivero, P. Anielski, W. Gawlik, and M. W. Mitchell, "Shot-noise-limited magnetometer with sub-picotesla sensitivity at room temperature," Rev. Sci. Instrum. **85**(11), 113108 (2014).
15. N. Wilson, P. Light, A. Luiten, and C. Perrella, "Ultrastable optical magnetometry," Phys. Rev. Appl. **11**(4), 044034 (2019).
16. D. Budker, D. F. Kimball, V. V. Yashchuk, and M. Zolotorev, "Nonlinear magneto-optical rotation with frequency-modulated light," Phys. Rev. A **65**(5), 055403 (2002).
17. S. Pustelny, A. Wojciechowski, M. Gring, M. Kotyrba, J. Zachorowski, and W. Gawlik, "Magnetometry based on nonlinear magneto-optical rotation with amplitude-modulated light," J. Appl. Phys. **103**(6), 063108 (2008).
18. F. Zhou, C. J. Zhu, E. W. Hagley, and L. Deng, "Symmetry-breaking inelastic wave-mixing atomic magnetometry," Sci. Adv. **3**(12), e1700422 (2017).
19. W. Qu, S. Jin, J. Sun, L. Jiang, J. Wen, and Y. Xiao, "Sub-hertz resonance by weak measurement," Nat. Commun. **11**(1), 1752 (2020).
20. N. Otterstrom, R. C. Pooser, and B. J. Lawrie, "Nonlinear optical magnetometry with accessible in situ optical squeezing," Opt. Lett. **39**(22), 6533–6536 (2014).
21. D. Budker, D. F. Kimball, S. M. Rochester, and V. V. Yashchuk, "Nonlinear Electro- and Magneto-Optical Effects Related to Bennett Structures," Phys. Rev. A **65**(3), 033401 (2002).
22. D. Budker, W. Gawlik, D. F. Kimball, S. M. Rochester, V. V. Yashchuk, and A. Weis, "Resonant nonlinear magneto-optical effects in atoms," Rev. Mod. Phys. **74**(4), 1153–1201 (2002).
23. D. Budker, D. F. Kimball, S. M. Rochester, and V. V. Yashchuk, "Nonlinear magneto-optical rotation via alignment-to-orientation conversion," Phys. Rev. Lett. **85**(10), 2088–2091 (2000).
24. D. F. J. Kimball, L. R. Jacome, S. Guttikonda, E. J. Bahr, and L. F. Chan, "Magnetometric sensitivity optimization for nonlinear optical rotation with frequency-modulated light: rubidium D2 line," J. Appl. Phys. **106**(6), 063113 (2009).
25. P. D. Kunz, D. H. Meyer, and F. K. Fatemi, "Twists in nonlinear magneto-optic rotation with cold atoms," Opt. Express **25**(14), 16392 (2017).
26. P. Bevington, R. Gartman, and W. Chalupczak, "Generation of Atomic Spin Orientation with a Linearly Polarized Beam in Room-Temperature Alkali-Metal Vapor," Phys. Rev. A **101**(1), 013436 (2020).
27. S. M. Rochester and D. Budker, "Atomic polarization visualized," Am. J. Phys. **69**(4), 450–454 (2001).
28. S. M. Rochester, "AtomicDensityMatrix Mathematica package," http://rochesterscientific.com/ADM/.
29. M. Auzinsh, D. Budker, and S. M. Rochester, "Light-Induced Polarization Effects in Atoms with Partially Resolved Hyperfine Structure and Applications to Absorption, Fluorescence, and Nonlinear Magneto-Optical Rotation," Phys. Rev. A **80**(5), 053406 (2009).